Comparison of X-ray and neutron tomographic imaging to qualify manufacturing of a fusion divertor tungsten monoblock

Ll.M. Evans[1,2,*], T. Minniti[3], M. Fursdon[1], M. Gorley[1], T. Barrett[1], F. Domptail[1], E. Surrey[1], W. Kockelmann[3], A. v. Müller[4], F. Escourbiac[5], A. Durocher[5]

[1]Culham Centre for Fusion Energy, Culham Science Centre, Abingdon, Oxon, OX14 3DB, UK

[2]College of Engineering, Swansea University, Bay Campus, Fabian Way, Swansea, SA1 8EN, UK

[3]STFC, Rutherford Appleton Laboratory, ISIS Facility, Harwell, OX11 0QX, UK

[4]Max-Planck-Institut für Plasmaphysik, Boltzmannstraße 2, 85748 Garching, Germany

[5]ITER Organization, Route de Vinon-sur-Verdon, CS 90 046, 13067 St. Paul Lez Durance Cedex, France

1. Abstract

Within a tokamak fusion energy device, the performance and lifespan of a divertor monoblock under high heat flux cycles is of particular interest. Key to this is the quality of manufacture, especially the material joining interfaces. Presented here is a comparative study between X-ray and neutron tomography to investigate the quality of manufactured monoblocks. Tungsten is a high attenuator of X-rays, thus X-ray tomography was performed on 'region of interest' samples where the majority of the tungsten armour was removed to reduce the attenuation path. Neutron tomography was performed on the full monoblock samples for non-destructive testing and on the 'region of interest' samples for direct comparison. Both techniques were shown to be capable of imaging the samples but having their own advantages and disadvantages relating to image accuracy and logistical feasibility. The techniques discussed are beneficial for either the research and development cycle of fusion component design or in quality assurance of manufacturing.

2. Introduction

The most common nuclear fusion energy device is the tokamak. Within this, the divertor plays a key role as an exhaust for helium, the waste product of the fusion reaction. This is accomplished by directing plasma along magnetic field lines to strike target plates within the divertor, see Figure 1 a). This component is therefore the one subjected to the greatest steady thermal load. During steady-state operation thermal fluxes are expected to be at least 10 MW·m^{-2}. This value could be surpassed if plasma disruptions which release large amounts of energy over short time periods are not mitigated [1]. It is proposed that the divertor will consist of a series of flat armour tiles aligned in rows, see Figure 1 b), with one side being plasma facing [2]. In order to remain within operational temperature limits the components are actively cooled. This is achieved by connecting the tiles through their centres to a pipe carrying coolant (coined a monoblock), see Figure 1 c). As the function of this heat sink is to transfer thermal energy away from the armour, it is imperative that the method of joining the armour to the pipe must provide a bond that retains both structural integrity and a high thermal conductivity under large thermal loads. As this region will contribute to, and potentially dominate, performance of the component, it is of utmost importance that the armour-pipe interface is well characterised.

---

[*] Corresponding author. Tel: +44 1235 465213. E-mail: llion.evans@ukaea.uk (Ll.M. Evans).
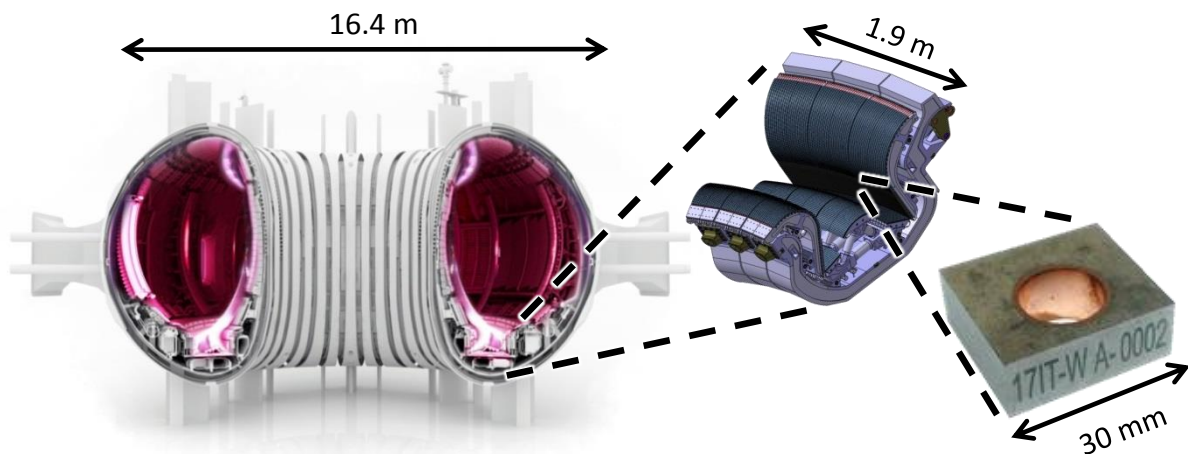
Figure 1. (a) Schematic of a fusion device [3]**, (b) the divertor region** [4]**, (c) photograph of divertor monoblock (tungsten armour around CuCrZr cooling pipe) which is subject to high heat flux and particle erosion.**

For ITER, the largest fusion device currently under construction, the monoblock will use tungsten (W) for the armour with a copper alloy (CuCrZr) cooling pipe. The armour is bonded to the pipe to maintain thermal conduction, but a large thermal expansion coefficient mismatch between the W and CuCrZr causes high levels of stress within the part. Therefore a functional compliant interlayer is used at the material interface to create a bond between the pipe and armour with improved longevity see Figure 2. For future devices, where it would be desirable to operate at higher thermal fluxes, alternatives designs are being investigated e.g. using composite materials, a functionally graded interlayer or geometric constructs [5]. It is estimated that ITER will use approximately 320,000 monoblocks in the divertor which will require replacing after 5 full power years (fpy) of operation due to degradation [6]. In addition to investigating alternative designs, various manufacturing routes are being tested which aim to reduce the cost of manufacturing e.g. bonding of the armour to heat sink materials via brazing rather than direct casting of copper.
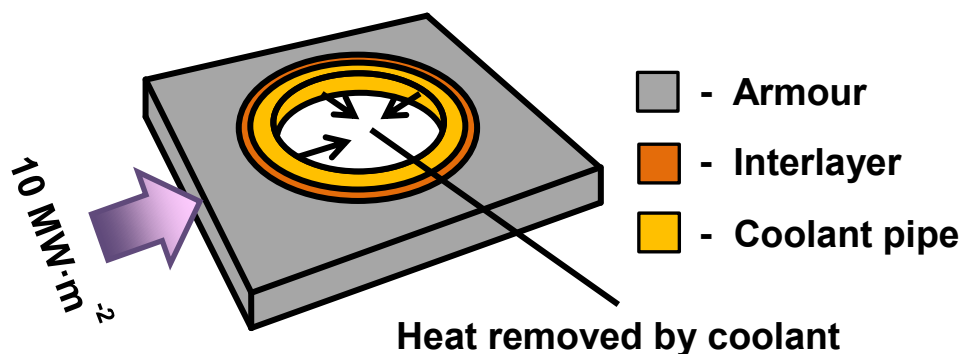

Figure 2. Schematic of divertor monoblock showing the main constituent regions and in service loads.

Because of this, the capability to inspect the material interfaces within the monoblock is of great value. This is true for both quality assurance, when manufacturing the current generation, and informing decisions in the development of next generation monoblocks. The features of concern in this region are anything that may reduce the component's lifespan by reducing its ability to withstand high thermal loads. For example, micro-cracking or voids will act as thermal barriers which can increase peak temperatures or act as crack or interface debonding initiation sites when experiencing thermal fatigue. Deviations from design tolerance cause differences between real and

predicted stress and temperature fields which may exceed safety limits. For this component, tolerances of interest are interlayer thicknesses and small-scale geometric constructs. For future designs which may include composite materials, the exact fibre placement or matrix permeation may be of importance due to localised variations in the material's performance leading to stress concentration zones or thermal hot spots. Finally, other features such as material inclusions or the flow of filler material from the brazing process is also of interest. A better understanding of the extent of the existence of these features will aid better informed decisions with regard to the suitability of particular manufacturing routes.

Currently the main methods for investigating manufacture quality of divertor monoblocks are via conventional optical or scanning electron microscopy (SEM) and ultrasonic scanning. SEM produces nanometre resolution images and may even be used to investigate compositional makeup e.g. elemental diffusion at material interfaces [7]. However, the technique is destructive as the sample must be cut in preparation of imaging. For brittle materials like tungsten this may introduce defects that were not present within the component. Additionally, two dimensional cross-sections showing features like cracks or inclusions provide insufficient data about the size and shape of features. Serial sectioning techniques may be used for additional data for the third dimension [8] but these are extremely time consuming and have relatively low resolution through thickness. Ultrasonic scanning is very effective in providing a relatively quick verification for the quality of bonding for the current generation design of monoblock. This technique scans radially around the coolant pipe by moving a transducer along the thin edges of the monoblock [9]. A drawback of the technique is its inability to distinguish between voids or inclusions as it only measured the changes in acoustic signal from a baseline value. It is also limited in its relatively low millimetre scale resolution and could not be used to investigate fine tolerance deviations. Additionally, geometric constructs or composite fibres in future generation designs will appear as changes in signal, these may be difficult to distinguish between against component defects. A recent development of this technique is to combine ultrasonic scanning and infrared imaging for improved defect detection [10].

A method which has been increasing in its use within an industrial setting is computerised tomography (CT). This has the benefit of providing three dimensional images which give data about features size and shape. This method depends on contrast in signal attenuation which means it is not well adept for interfaces between similar materials, e.g. carbon fibres in a carbon matrix, but can easily distinguish between voids and inclusions and even determine interfaces between differing metals if there is sufficient attenuation contrast [11].

Various CT techniques use different signals which are appropriate for the medium being imaged e.g. radio signals are used for upper atmosphere studies [12]. For industrial manufacturing the most common method is X-ray tomography [13]. Depending on the precise setup this can provide nanometre resolution but is typically on the micron scale for commonly available commercial scanners [11]. The main challenge with using X-ray tomography for imaging of the divertor monoblock is that tungsten is an extremely high attenuator of X-rays. Previous work shows use of synchrotron X-rays on cylindrical tungsten samples with a diameter of 0.5 mm and states that this was the achievable limit [14]. This is relatively small in comparison to the proportion of a monoblock that would be required to provide significant data about the material interfaces. However, recent advances in CT hardware offer higher energy X-rays than previously available which may be sufficient to image portions of the monoblock providing significant data.

Other than X-ray CT, neutrons could provide viable CT signal sources that aren't attenuated excessively by tungsten to such a level that impedes imaging. Neutron CT is a relatively immature technique and can only be performed at a handful of facilities globally [15]. Additionally, when the samples interact with the beamline they become activated. Depending on the materials used in the samples the time required for the samples to reduce sufficiently in activity may be prohibitive in the feasibility in their wide-scale use for component qualification. The neutron damage from the beamline will be insignificant compared of in service use and can therefore be disregarded. Depending on the level of detail provided by this technique the benefits could far outweigh the disadvantages.

This paper investigates and compares the advantages and disadvantages of X-ray and neutron CT imaging of current and future generation divertor monoblocks. This includes the quality of the images themselves, detailing characteristics such as resolution and noise, and the logistical feasibility requiring consideration due to steps such as sample preparation.

3. Sample manufacturing

For this study three sample types were used: ITER reference monoblock (ITER_MB), Culham Centre for Fusion Energy thermal break concept monoblock (CCFE_MB) and Max-Planck-Institut für Plasmaphysik tungsten fibre / copper matrix coolant pipe (IPP_Wf-Cu), as shown in Figure 3.
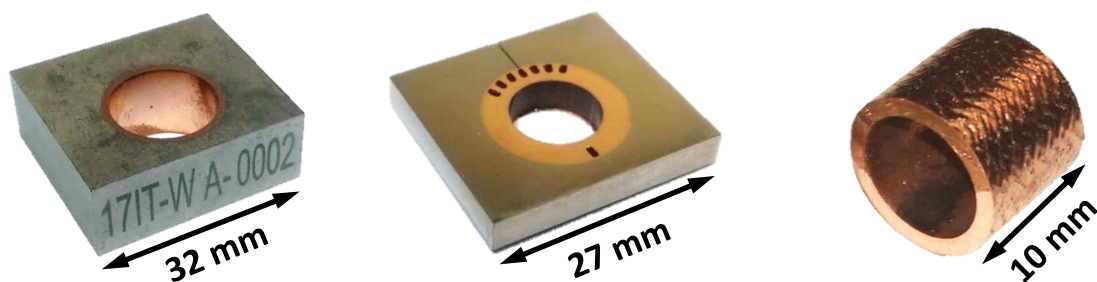

Figure 3. Three sample types used for this work: (left) ITER reference monoblock (ITER_MB), (centre) Culham Centre for Fusion Energy thermal break concept monoblock (CCFE_MB) and (right) Max-Planck-Institut für Plasmaphysik tungsten fibre / copper matrix coolant pipe (IPP_Wf-Cu)

The 'ITER_MB' sample is manufactured by first producing a bar of sintered tungsten which is rolled to yield elongated grains whose longitudinal orientation are aligned such they shall not be parallel to the surface. The tungsten armour is then machined to shape before oxygen free high conductivity (OFHC) copper is directly cast into the internal hole. A drill is then used to machine the copper layer to leave the desired interlayer thickness. For use within the divertor, a series of monoblocks would be placed along a copper alloy (CuCrZr) coolant pipe and joined by hot radial pressing. The main ITER_MB sample used in this instance only included the armour and interlayer. A second sample, 'ITER_HHFT', which had been subjected to high heat flux testing prior to imaging also included the coolant pipe.

The 'CCFE_MB' sample was fabricated using a two-stage vacuum braze process. Copper sleeves (for interlayer material) were first brazed to CuCrZr pipes and the geometric constructs (grooves) machined into the outer surface of the subsequent assembly. Tungsten monoblocks were cast with copper into the central bore (with similar specifications to the ITER_MB sample). This was then machined out to leave a thin copper layer. A stress relieving slit was cut into the plasma facing surface of the tungsten by electro-discharge machining (EDM). A second Cu-to-Cu braze process was

performed where the W/Cu blocks are attached to the pipe/sleeve assembly to create the complete mock-up component. The final braze also included a precipitation hardening cycle. The braze filler material used was a 50:50 Au-Cu foil, known commercially as Orobraze 970, which had a thickness of 25 μm and was wrapped around the inner part three times before bonding. For more details on the design and manufacture of the monoblock see [16].

For the 'IPP_Wf-Cu' sample, the W fibre preform used was manufactured by means of sequential circular mandrel overbraiding. The raw material used were drawn potassium (K) doped W fibres with a nominal diameter of 150 μm. The resulting preform comprised 5 braided layers which exhibited a regular 2/2 twill weave repeat pattern. The W_f-Cu composite material was then produced by infiltrating the braided preform with liquid Cu. Eventually, the infiltrated composite was machined to final dimensions (inner diameter: 10 mm, wall thickness: 1.5 mm) and specimens with an axial length of 10 mm were cut. For further detail on the manufacturing and the motivation for interest in W_f-Cu materials for this application see [17].

4. Methodology

All radiographic methods, using different type of radiations such as X-rays or neutrons, are based on the same general principle: that radiation is attenuated on passing through matter [18]. The object under examination is placed in the incident radiation beam. After passing through, the beam that remains enters a detector that registers the fraction of the initial radiation intensity that has been transmitted by each point in the object. Inhomogeneities in the object or an internal defect (e.g. void, crack, porosity or inclusion) will show up as a change in radiation intensity reaching the detector. Thus detection of defects in radiography is based on the observation of differences in radiation intensity after passing through the object under examination. This occurs according to the the Beer-Lambert law, see Equation (1), where I_0 and I are the incident and attenuated intensities, respectively, μ is the linear attenuation coefficient of the material (combining the interaction cross-section and nuclear density) and s is the path length through the sample.

$$I(x,y) = I_0(x,y)e^{-\int_{path} \mu(x,y,z)ds}$$

(1)

As can be seen from Equation (1), radiography provides line-integrated information related to the amount of attenuation where contributions from different elements and the amount of material corresponding to the path length cannot be separated. However, in tomography one collects multiple radiographies (projections) for distinct angular orientations of the sample with respect to the incident radiation beam. From the tomographic scan, one obtains three-dimensional spatially resolved images (i.e. volumetric data), which generally display the attenuation coefficient distribution in the sample volume. This procedure makes use of different reconstruction algorithms, such as filtered back projection (FBP) or iterative based algorithms [18].

4.1. X-ray tomography sample preparation and scanning

Because tungsten's has extremely high X-ray attenuation levels, a sufficiently long tungsten attenuation path would reduce the X-ray signal source such that it would not be possible to gather sufficient data to perform a volumetric reconstruction. To reduce the attenuation path length 'region of interest' (ROI) samples were produced by using electro discharge machining (EDM) to

remove the majority of the tungsten armour. The aim was to leave a tungsten layer sufficiently thick such that the EDM cut would not affect the material interfaces but thin enough to allow full X-ray penetration. The resultant ROI sample dimensions are shown in Table 1. A schematic of the scanning setup and resultant ROI sample can be seen in Figure 4. Photographs of the samples are shown in Figure 5. To further reduce the attenuation path length, the sample was scanned at a ~45° tilt angle relative to the centreline between the X-ray source and detector.

Unlike neutron tomography, industrial X-ray CT is now a well-established technique, therefore detailed methodology and hardware specifications can readily be found elsewhere e.g.[19], [20]. Scanning was performed using commercially available industrial scanners and followed standard industrial X-ray CT practice. The parameters used for each scan are shown in Table 2. Reconstruction of the 3D volume from 2D radiographs was completed using CT Pro V3.1 (Nikon Metrology NV, Tring, Hertfordshire, UK).
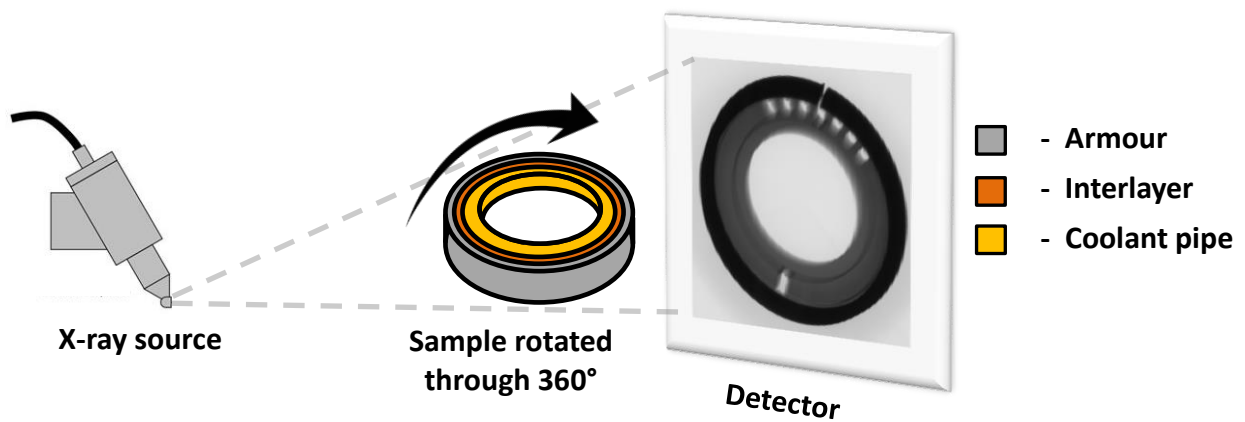

Figure 4. Schematic of X-ray tomography setup using region of interest sample

Table 1. Dimensions of region of interest samples.

Sample	ID/OD Diameter (mm)	Pipe thickness (mm)	Tungsten thickness (mm)	Length (mm)	Material
ITER_MB_ROI	15/19	2	1	5	W-Cu
ITER_HHFT_ROI	12/17	2.5	0.5	3	W-Cu-CuCrZr
CCFE_MB_ROI	10/18	4	0.5	2	W-Cu-Cu-CuCrZr
IPP_Wf-Cu	10/13	1.5	0.15 fibres	10	W_f-Cu fibre composite

Figure 5. Photographs of 'region of interest' samples. Clockwise from top left: ITER_MB_ROI, ITER_HHFT_ROI, IPP_Wf-Cu, CCFE_MB_ROI.

Table 2. X-ray tomography scanning parameters.

Sample	Machine	Voltage (kV)	Current (μA)	Filter (mm)	Acquisition time (s)	Number of projections	Frames / projection
ITER_MB_ROI	NSI X5000	240	100	N/A	500	1440	3
ITER_HHFT_ROI	NSI X5000	240	100	N/A	500	1440	3
CCFE_MB_ROI	Nikon 225	220	80	Cu, 0.5	1000	3142	1
IPP_Wf-Cu	Nikon 225	200	220	Cu, 2.0	500	2616	1

4.2. Neutron tomography scanning

For the implementation in this study, the advantage neutron imaging has in comparison to X-ray imaging is that neutrons are significantly more penetrating through tungsten. Thus, it is feasible to image samples containing larger volumes of tungsten. For this work, the importance is that full monoblock samples may be scanned. Neutron tomography was performed at IMAT, ISIS, Rutherford Appleton Laboratory, STFC, UK [21], [22].

In practice the setup for neutron and X-ray tomography is very similar. The sample is placed in between the radiographic source and detector, it is rotated through 360° whereby a series of 2D radiographs are taken at uniformly spaced angular steps, as previously shown in Figure 4. Other than the radiographic source, the main difference between these two setups is that the neutron imaging uses a quasi-parallel beam rather than a cone angle beam geometry (although a parallel setup is also possible for X-ray imaging). Parallel beam geometry is realised in a neutron imaging facility like IMAT with a pinhole selector system. Neutrons are forced to propagate, downstream of the neutron guide, through a circular aperture with diameter D before being detected after a distance L by the neutron camera. This produces a specific beam divergence or collimation ratio L/D. The sample position at IMAT has a distance L of about 10 m. Depending on the specimen characteristic and boundary conditions (neutron flux, spatial resolution of the detector, etc.) such collimation ratio could be change on IMAT to 125, 250, 500, 1000 and 2000 by changing the pinhole diameter [21]. A large L/D value means a low beam divergence and neutron flux and vice versa [23]. Another important aspect of a parallel beam setup is the maximum distance, l, of the object from the imaging detector. In fact every point in a sample is scaled up to an area with the diameter $d = l/(L/D)$ at the detector plane. This geometrical blurring effect was the dominant contribution

in the tomography scans performed here on the final spatial resolution. A collimation ratio L/D of 250 was used with a 40 mm pinhole diameter.

The imaging camera used has a maximum exposure time of 30 s because it is not actively cooled. Although larger L/D ratios may usually be selected to improve the final spatial resolutions, this detector limitation prevented this possibility. That is, the fixed maximum exposure time set the maximum signal to noise ratio (SNR) achievable for each L/D configuration and neutron flux. The settings used were considered the best compromise between spatial resolution and SNR in the final radiographs. Low noise (actively cooled) imaging camera with longer exposure capabilities should overcome this issue which is a solution is currently under developments on the instrument.

A neutron beam size at sample position of ~70x70 mm^2 was used to irradiate all the samples. Radiographs were collected using a CMOS neutron tomography camera [24]. The camera had a 2048 x 2048 pixel sensor, with a sensitive area of 59.5x59.5 mm^2 at the neutron-sensitive scintillator screen. The scintillator screen (50 μm thick 6LiF:ZnS) "converts" neutrons into visible light while preserving their 2D distribution; the CMOS device takes images of the emitted light through an objective lens system positioned at 90° with respect to the neutron beam. For each measurement, multiple radiographs were acquired along with periodic dark and flat field images at an integration time of 30 s each. The dark field, I_{dark}, and flat field, I_0, images were used for normalization purpose to represent the attenuation of the beam instead of an intensity reading. The dark and flat field images are taken when the beam is off and on, respectively, while the sample is out of the beamline to account for camera noise and beam inhomogeneities. For each data type (sample, flat and dark field) an average of ten different radiographs were required to improve neutron statistics and noise reduction. The normalised image was calculated as shown in Equation (2).

$$I_{norm} = \frac{I - I_{dark}}{I_0 - I_{dark}}$$

(2)

The full monoblock samples shown in Figure 3 a) and b) were scanned whilst mounted in a 45° tilt position to minimise the attenuation path length. The dimensions for these samples are shown in Table 3. Additionally, the ROI samples were scanned for a direct comparison with the X-ray tomography scans detailed in section 4.1. Because of the neutrons' relatively higher penetration capability it was possible to scan the samples in the flat position i.e. 0° tilt. This made is possible to image all four samples (ITER_MB_ROI, ITER_HHFT_ROI, CCFE_MB, IPP_Wf-Cu) in one scan by stacking them on top of each other.

For the ROI samples, ITER_MB and CCFE_MB the number of projections taken were 707, 1204 and 1333 respectively. Each projection used the maximum acquisition time of 30 s. Reconstruction of the 3D volume from 2D radiographs was completed with a standard filtered back-projection algorithm using Octopus Imaging Software (XRE NV, Gent, Belgium).

Table 3. Dimensions of the monoblock samples.

Sample	Height (mm)	Width (mm)	Depth (mm)	Material
ITER_MB	28	32	5.5	W-Cu

| CCFE_MB | 24 | 27 | 4 | W-Cu-Cu-CuCrZr |

4.3. Image processing

CT data output essentially consists of a series of 2D image 'slices' comprising greyscale pixels, e.g. Figure 6. Each slice has a thickness attributed to it; often equal to the width and height of the 2D pixel, thus a 3D pixel (voxel) is formed. When the slices are stacked together these represent a 3D volume. All visualisation and analysis of the tomographic volumes was undertaken using the software Fiji [25]. This is a specific distribution of ImageJ [26] which includes plugins specifically to facilitate scientific image analysis.

5. Results

Because the X-ray tomography used a cone beam source, moving the sample closer to the source magnifies the image on the detector which can be used to achieve smaller voxel widths. Whereas the neutron beamline at IMAT uses an approximately parallel beam which means that resultant voxel widths weren't sample dependent, but rather on the neutron setup of the pinhole and detector. Considering these factors the voxel widths for each scan can be calculated, as shown in Table 4. It should be noted that the minimum resolvable feature size is not directly related to voxel widths alone because it is also a complex function of any intrinsic noise or scanning artefacts within the image. For the neutron CT the geometrical unsharpness, d, (also shown in Table 4) is quantifiable by the relationship between the maximum distance of the sample from the detector, l, and the L/D ratio.

Table 4. Resultant image qualities considering scanning parameters.

Sample	X-ray CT	Neutron CT		
	Voxel width (µm)	Voxel width (µm)	Maximum distance l (mm)	Geometrical unsharpness d (µm)
ITER_MB_ROI	12.4	29	25	100
ITER_HHFT_ROI	11.7	29	25	100
CCFE_MB_ROI	10.9	29	25	100
IPP_Wf-Cu	12.6	29	22	88
ITER_MB	N/A	29	44	176
CCFE_MB	N/A	29	43	172

Figure 6-Figure 9 are example cross sectional slices from the tomography data sets for the ROI samples. In each figure the top row is a slice approximately midway along the pipe length (xy plane) and the bottom row is a slice in the xz plane. The left and right columns show data from the X-ray and neutron tomography data, respectively.

Figure 10 shows example cross sectional slices from the neutron tomography data sets for the full monoblock samples. The top and bottom rows show the xy and xz planes, respectively, and left and right columns show the ITER_MB and CCFE_MB samples, respectively.
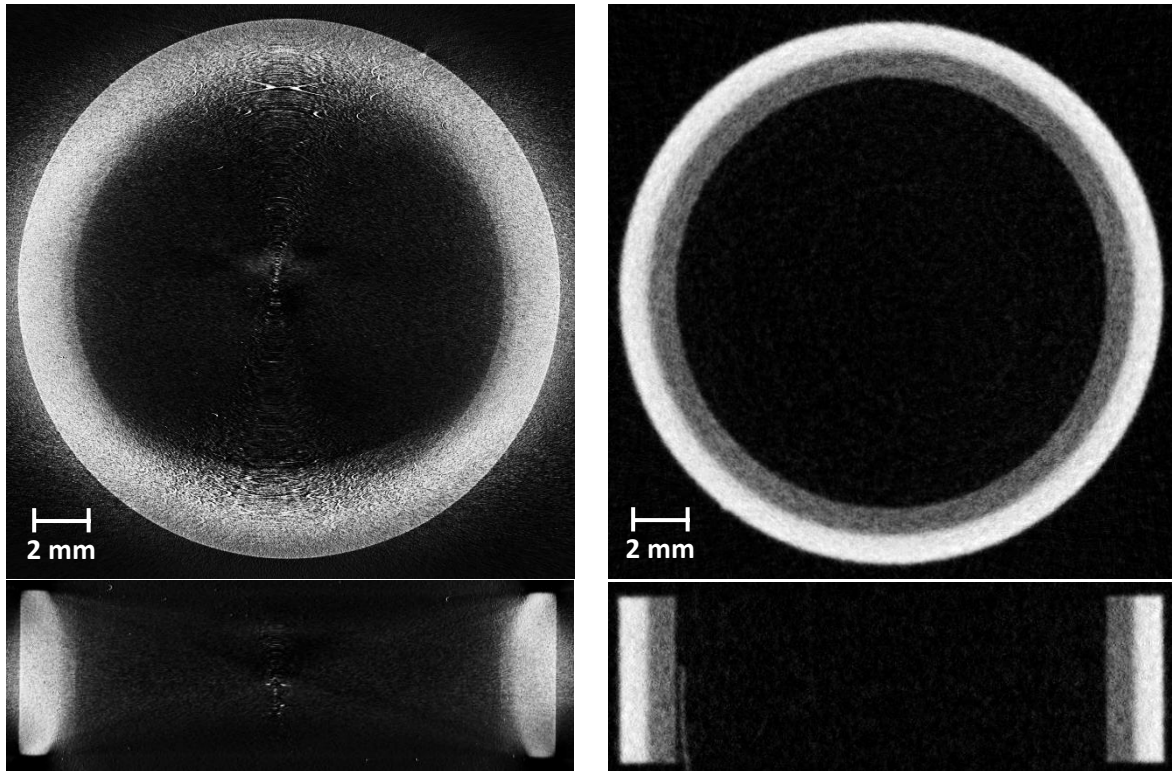
Figure 6. Example cross sectional tomography data slices from the xy (top) and xz (bottom) planes for the ITER_MB_ROI sample with a comparison of X-ray (left) vs. neutron (right) tomography imaging results.
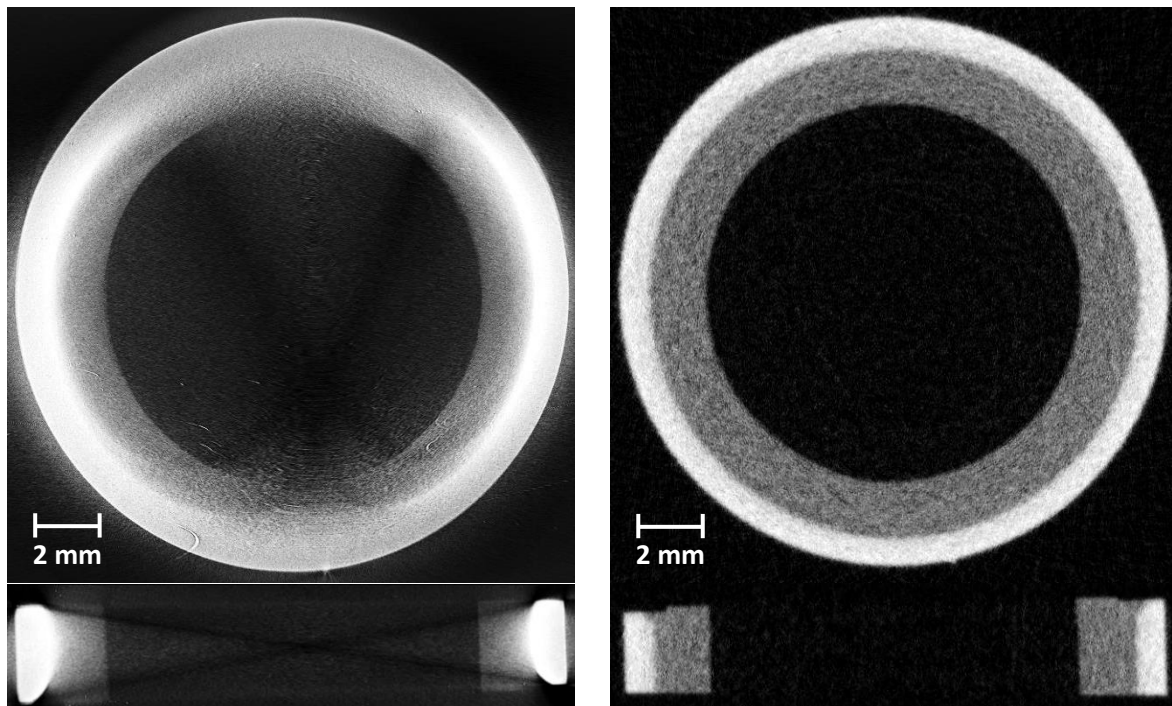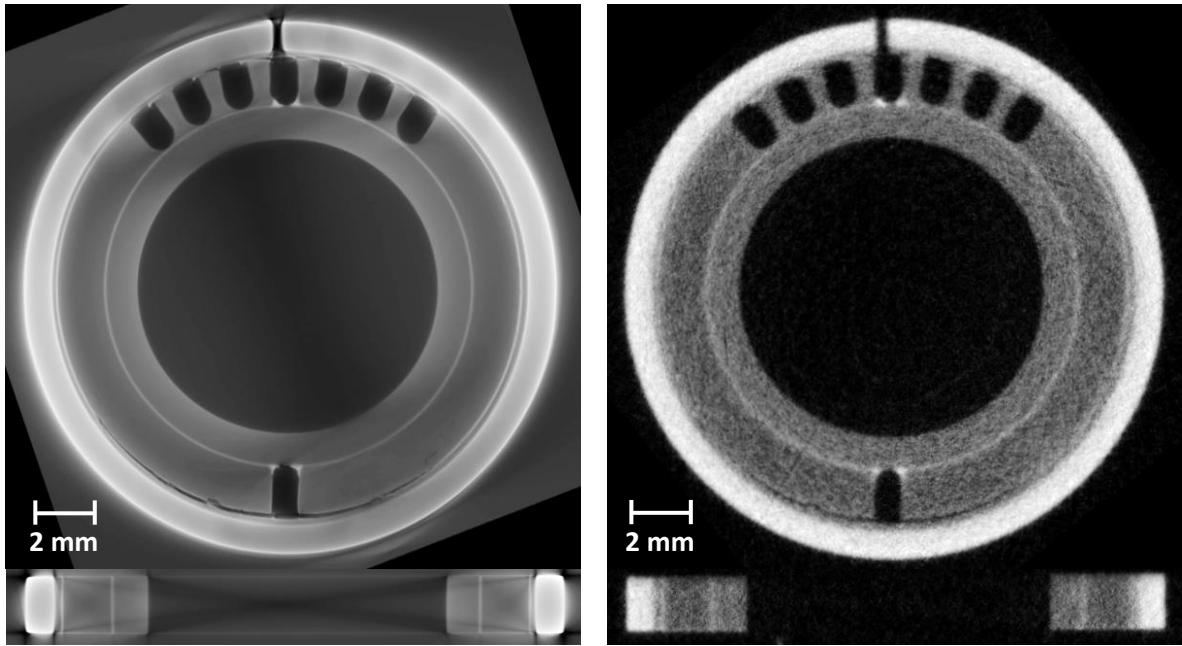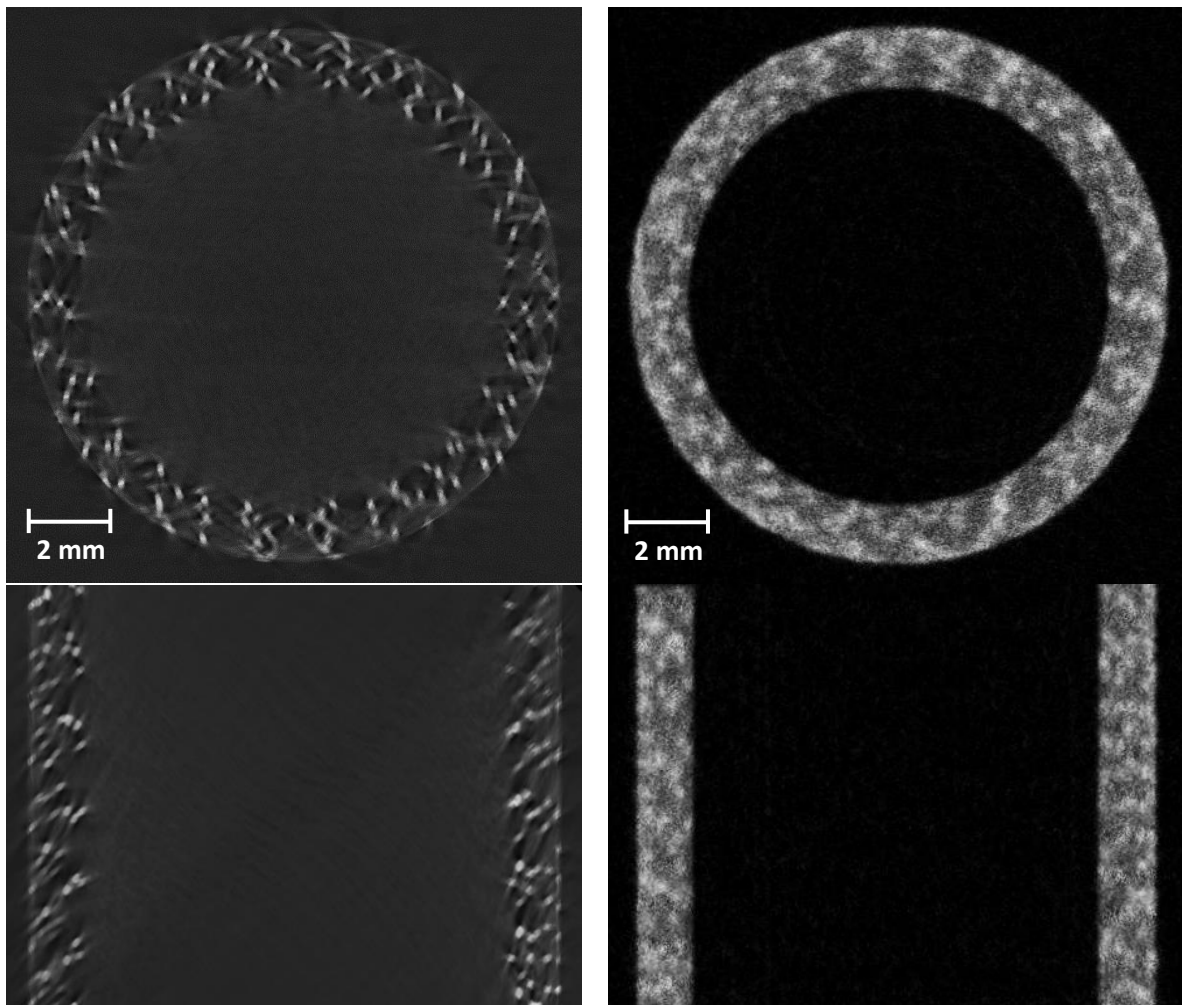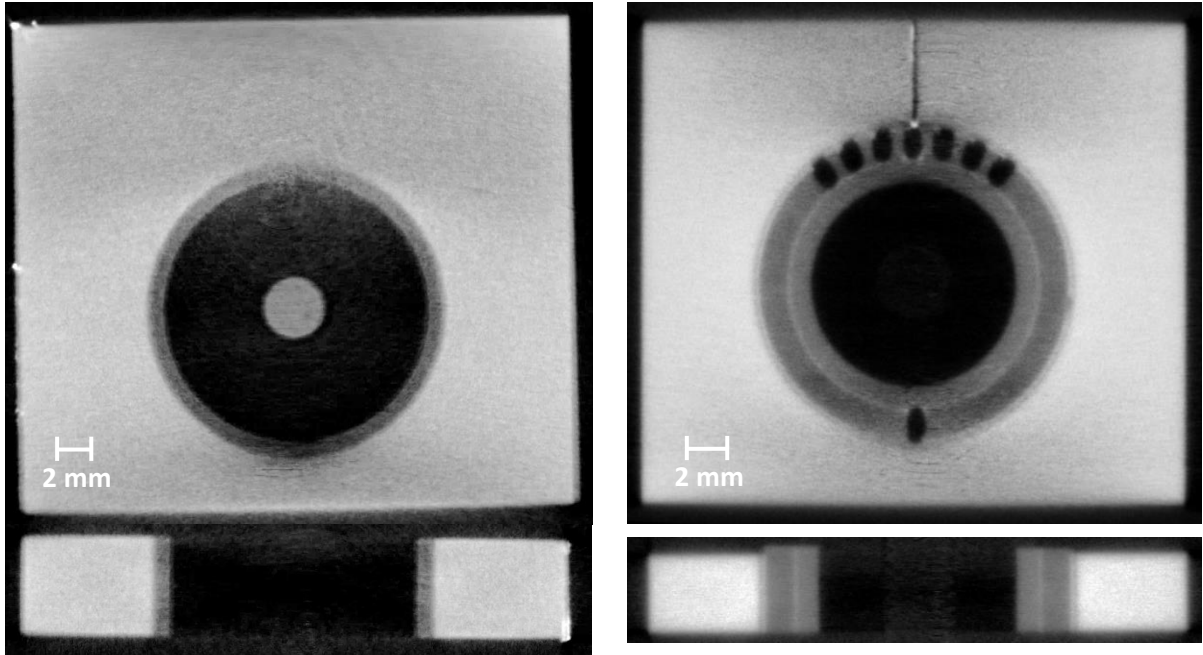

Figure 7. Example cross sectional tomography data slices from the xy (top) and xz (bottom) planes for the ITER_HHFT_ROI sample with a comparison of X-ray (left) vs. neutron (right) tomography imaging results.

Figure 8. Example cross sectional tomography data slices from the xy (top) and xz (bottom) planes for the CCFE_MB_ROI sample with a comparison of X-ray (left) vs. neutron (right) tomography imaging results.

Figure 9. Example cross sectional tomography data slices from the xy (top) and xz (bottom) planes for the IPP_Wf-Cu sample with a comparison of X-ray (left) vs. neutron (right) tomography imaging results.

Figure 10. Example cross sectional neutron tomography data slices from the xy (top) and xz (bottom) planes for the ITER_MB (left) and CCFE_MB (right) samples.

6. Discussion

6.1. Samples

Because each of the samples is different it is worth to first consider these differences and their potential impact on results. Using the sample dimensions, the total volumes and the volumes of the constituent parts were calculated, as shown in Table 5. The column for Cu denotes the combination of pure Cu and Cu alloys. The fibre volume fraction for the IPP_Wf-Cu sample was estimated to be 10 %, therefore the constituent part volumes are based on this assumption because they could not be calculated geometrically. Also included are details about X-ray attenuation path length through the samples (the 'chord' and 'max. path' columns) which are discussed in greater detail later in this section.

Table 5. Volume of samples and constituent parts as calculated geometrically.

Sample	Volume (mm^3)	W Volume (mm^3)	Cu Volume (mm^3)	Chord (mm)	Max. path (mm)
ITER_MB_ROI	534	283	251	8.49	9.85
ITER_HHFT_ROI	342	78	264	5.74	6.48
CCFE_MB_ROI	352	55	297	5.92	6.24
IPP_Wf-Cu	542	54	488	8.31	13
ITER_MB	3956	3680	276		
CCFE_MB	2278	1684	594		

It is important to consider the quantity of material (particularly tungsten) in each sample because this is what attenuates the signal. As the levels of attenuation increases, the ability to acquire 'clean' images becomes more challenging due to a decreasing signal penetration. By comparing the tungsten volume in the three ROI samples it can be seen that for ITER_MB_ROI it is 3.6 and 5.1 times greater than ITER_HHFT_ROI and CCFE_MB_ROI, respectively.

However, the volume itself isn't a wholly accurate indicator of attenuation because a sample with evenly distributed attenuation paths across the detector is likely to be less challenging to image than a sample containing highly attenuating paths at particular angles. Thus, by considering the samples' maximum chord length, c, the maximum attenuation path through tungsten, p, was calculated, see Figure 11 and Table 5. Again the value for ITER_MB_ROI is greater than the other two samples. It can be seen that the chord for ITER_HHFT_ROI is less than that of CCFE_MB_ROI, but because of the sample's length, the maximum attenuation path is therefore greater. Considering the volumes of tungsten and the maximum attenuation paths through tungsten it is predicted that ITER_MB_ROI will pose the greatest imaging challenge followed by ITER_HHFT_ROI, then CCFE_MB_ROI.

Figure 11. Schematic showing maximum chord length, c, through tungsten section of ROI samples and maximum attenuation path, p.

For IPP_Wf-Cu it is difficult to estimate the maximum attenuation path through tungsten because the precise location of the fibres is unknown. The chord length and maximum attenuation path have been included in Table 5 as indicative values, but the majority of this will be through copper. However, given the estimate of tungsten volume it is likely that the sample will pose a similar imaging challenge to that of CCFE_MB_ROI.

The full monoblock samples (ITER_MB and CCFE_MB) contain considerably more tungsten than the ROI equivalents. The attenuation of X-rays through this volume of tungsten would have impeded X-ray tomography scanning, which is why it was decided to image these samples by neutron tomography only. Here it can be seen that the ITER_MB contains significantly more tungsten than the CCFE_MB sample indicating that it poses the greatest imaging challenge.

6.2. X-ray tomography

The minimum resolvable feature of a tomography image is a result of the combination of the image's voxel widths (due to scanning parameters as mentioned above) and the level of signal noise and reconstruction artefacts. In an ideal image it would require a minimum of three voxels to resolve a feature i.e. 0-1-0 for binarised data. In practice it typically requires 5-10 pixels, depending on the level of noise and artefacts. Following this rationale, according to the voxel widths shown in Table 4, it should be possible to resolve features with a minimum size of 50-100 μm for the X-ray tomography scans of the ROI samples.

When considering the ITER_MB_ROI sample it can be seen that the presence of reconstruction artefacts is sufficiently significant that it is not possible to distinguish the W-Cu interface (see Figure 6). Due to this, it is not possible to observe any features which may be present at the interface. Therefore, despite the voxel width being 12.4 μm, the minimum resolvable feature is orders of magnitude bigger. In practice the images from this scan is of no value for quantitative analysis and little value for qualitative analysis. Similarly, the same is true for the ITER_HHFT_ROI (see Figure 7).

The CCFE_MB_ROI sample has much improved definition such that the W-Cu interface is clearly seen. The improved feature visibility in this sample is due to the reduced X-ray attenuation path caused by the smaller amount of W present in the sample. This confirms the prediction made in section '6.1 Samples', where the maximum X-ray path through W was estimated, that the CCFE_MB_ROI sample would produce the image with least noise and artefacts because of the sample composition and geometry.

Observable features on the external surfaces of the CCFE_MB_ROI sample were compared with measurements made by optical microscopy. Examples of such features are cracking and braze layer thickness at the 'CuCrZr pipe-interlayer' and 'interlayer-Cu coating' interfaces. By this method it was ascertained that the signal noise and scanning artefacts were sufficiently low in this tomographic image that features of the order of 60 μm were resolvable. That is, features which are greater in size than ~6 voxels can be observed which confirms the previous assumption. Each layer of the sample can be distinctly observed, from inside to out. That is CuCrZr coolant pipe; braze; Cu interlayer; braze; cast Cu layer; W armour. Examples of internal features of observable interest are shown in Figure 12.

By taking a profile line through a central tomography slice it was possible to quantify the variation in greyscale through the constituent parts of the sample, shown in Figure 13. Here it can be seen that there are peaks at the CuCrZr-Cu and Cu-Cu interfaces and also at the edges of the W layer. The peaks at the Cu interfaces are due to the higher attenuation of Au in the braze filler material. The widths of these peaks are representative of the expected 75 μm thickness of the braze material. The peaks at the W edges are caused by the well-known phenomenon of beam hardening. This occurs when polychromatic beams are used and the soft X-rays (lower energy) are filtered by the sample giving the false appearance of a change in attenuation through the sample. That is, the change in greyscale through the W is not caused by a change in the material (e.g. density) but rather an artefact of the imaging technique. This should be taken into consideration when interpreting the images as it can lead to overestimating layer thicknesses. It is also worth noting that the contrast in greyscale levels of the CuCrZr and Cu layers is very low. Therefore, without the presence of the more highly attenuating braze at the interface it might be challenging to identify features in this region.

An additional image in the xz plane is shown in Figure 14. Here, edge streaking artefacts are clearly observed, in particular from the W armour. Streaking artefacts typically happen when undersampling occurs which would explain why it is most pronounced around the W armour. On the edges this can be seen to have a blurring effect on the higher greyscale levels that makes it more difficult to accurately distinguish the material boundary, as seen in the gradual decrease of greyscale level in the profile in Figure 13. At the corners, the opposite is true, where the artefact causes the corners to appear 'filleted' or 'smoothed off'. Both these imaging effects must be considered when attempting to make quantitative metrology measurements of the sample. The other parts of the sample can be seen to be less affected.
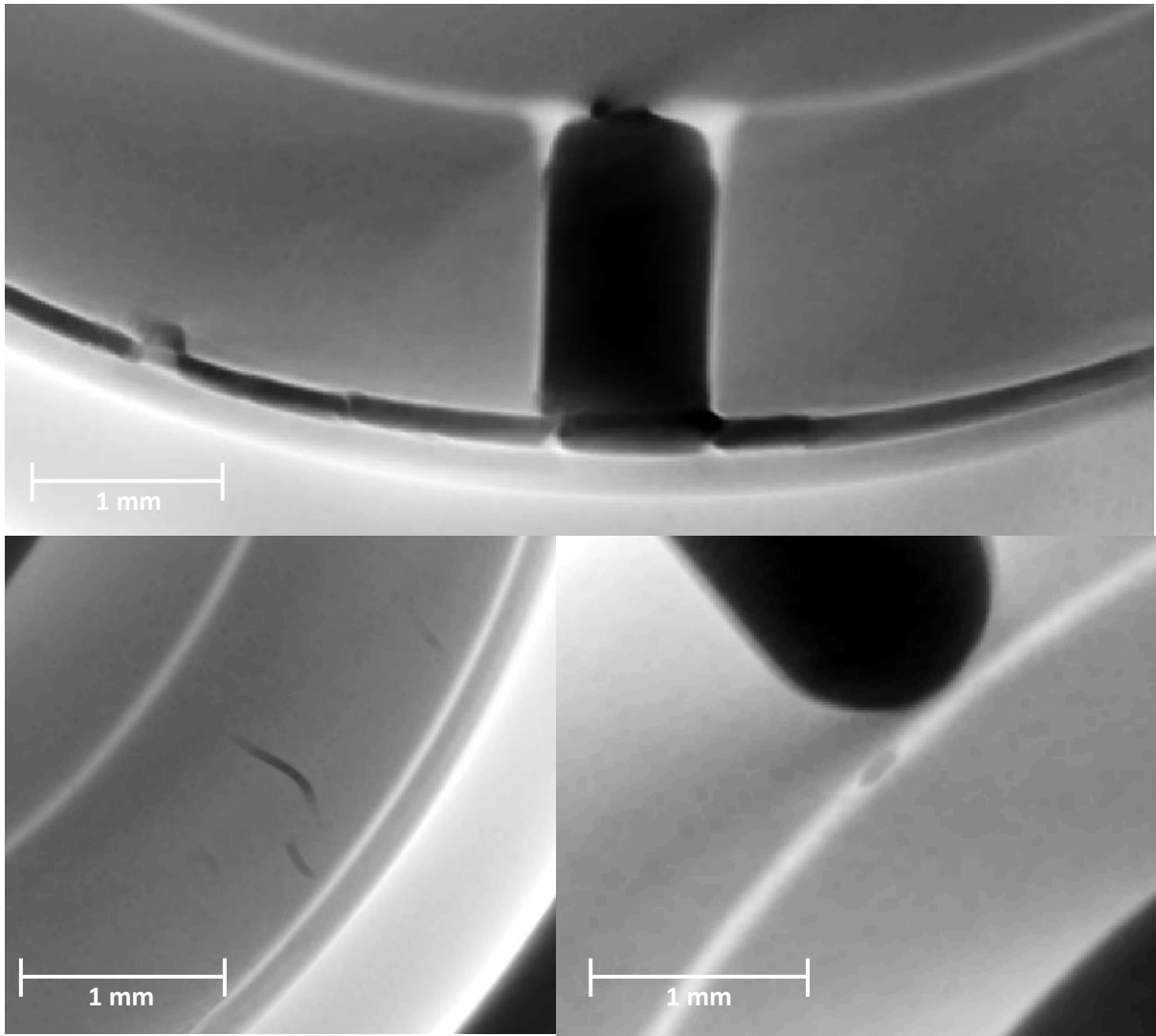
Figure 12. Zoomed in xy plane images from a X-ray tomography image of the CCFE_MB_ROI sample showing (top) debonding and variation in braze layer thickness, (bottom left) radial micro-cracking in Cu interlayer and (bottom right) pore within braze layer.
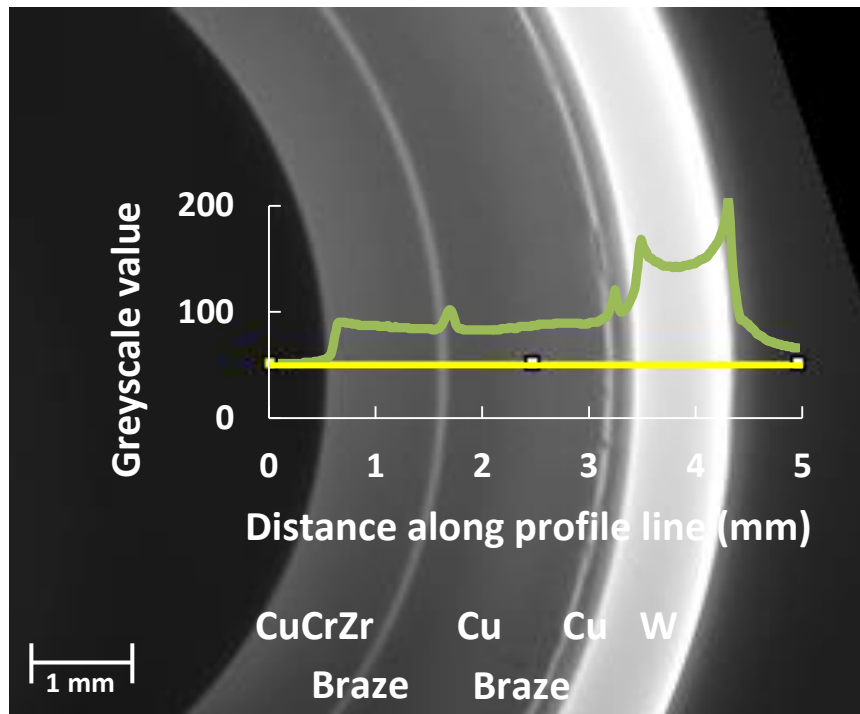
Figure 13. Plot of greyscale values (green) with respect to distance along profile line (yellow). Plot is overlaid on tomographic slice where profile was taken to show direct relation between changes in greyscale and image features.
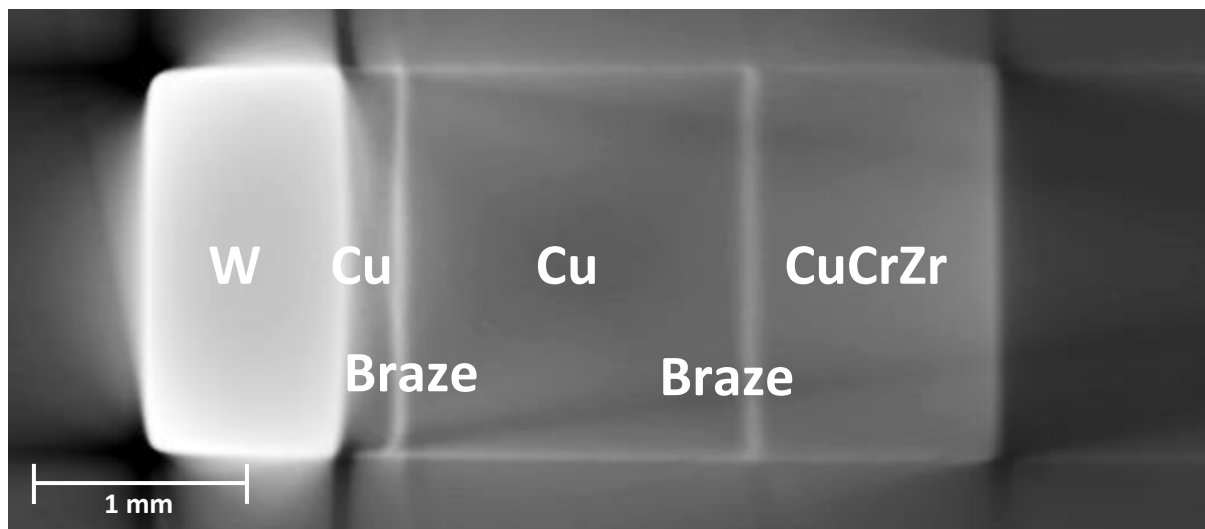

Figure 14. Zoomed in xz plane image from a X-ray tomography image of the CCFE_MB_ROI sample.

The 'quality' of the resulting image from the scan of the IPP_Wf-Cu sample (see Figure 9) was an improvement over the ITER_MB_ROI and ITER_HHFT_ROI samples but not as clear as the CCFE_MB_ROI sample. The resulting voxel width of this scan was 12.6 µm which was sufficient to distinguish the individual composite fibres which had a diameter of 150 µm. However, the high signal attenuation contrast between the W fibres and Cu matrix created a particular challenge in capturing detail within the Cu phase of the composite. It can be seen that there is low contrast in greyscale values between the Cu matrix and the surrounding background air which means that the sample boundaries are not well defined. In addition to this, streaking artefacts are prominent from each of the W fibres (see Figure 15). To quantify the variation in greyscale through the constituent parts of the sample a profile line through a central tomography slice is shown in Figure 16. In

addition to demonstrating the similarity in greyscale values of Cu and background phases it can be seen that the streaking artefacts in fact cause zones within the Cu matrix to appear less attenuating than the background, as shown by the troughs in the plot.

In practicality, the result of these artefacts is that it is challenging to utilise this image for investigation of micro-features at the fibre-matrix interface or to perform metrology quantifications. Despite this, the clear definition of the fibres means that centreline of each fibre can easily be found and visualised to investigate deviation of fibre placement from the ideal weave pattern. Figure 17 is a 3D visualisation of the fibre placements which can be viewed interactively using the post-processing software. Visualising the image along radial slices allows investigation of the weave pattern in the cylindrical coordinate space as shown in Figure 18.

Figure 15. Zoomed in xy plane image from X-ray tomography image of IPP_Wf-Cu sample demonstrating that individual fibres are resolvable to locate positioning. Also shown is a lack of contrast between Cu matrix and background air; also streaking artefacts from W fibres are visible.
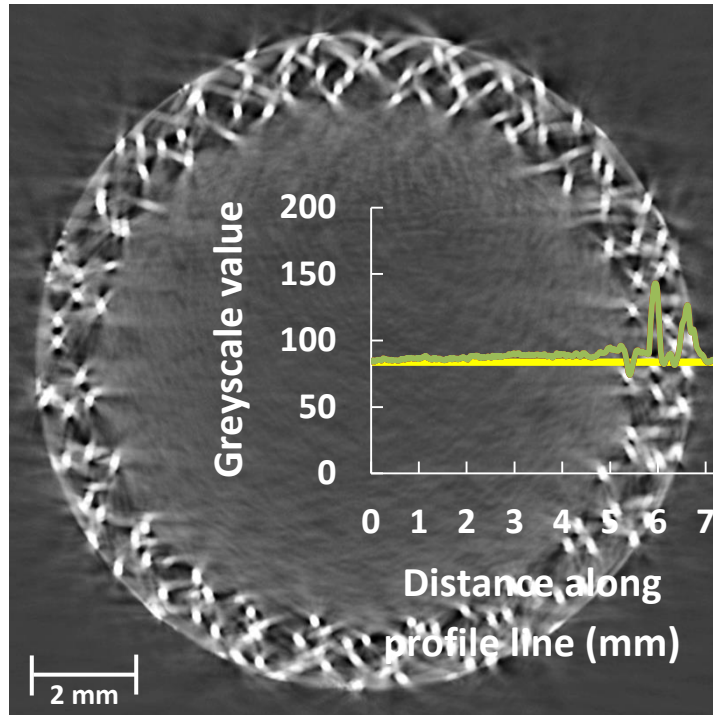
Figure 16. Plot of greyscale values (green) with respect to distance along profile line (yellow). Plot is overlaid on X-ray tomographic slice where profile was taken to show direct relation between changes in greyscale and image features.
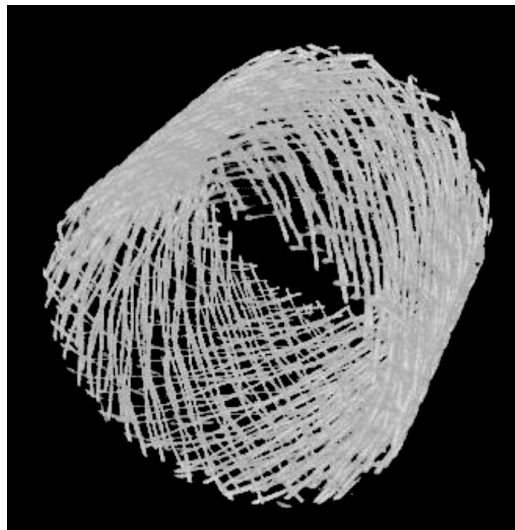

Figure 17. 3D visualisation from X-ray tomography data of W fibre placement within IPP_Wf-Cu sample, Cu matrix has been made transparent to assist viewing.
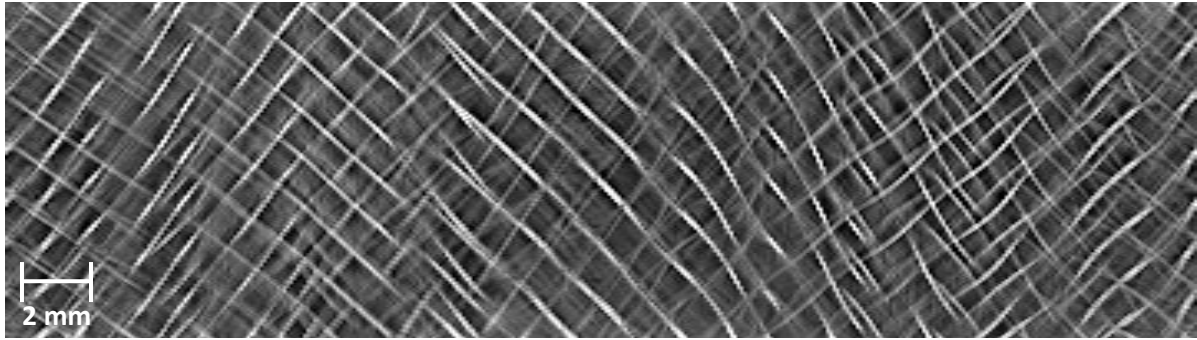
Figure 18. 'Unrolled' section from X-ray tomography image of IPP_Wf-Cu sample at radius = 5.75 mm (i.e. x-axis is along θ and y-axis is along length of pipe).

6.3. Neutron tomography

For the neutron tomography the three ROI samples and the IPP_Wf-Cu sample were scanned together. The same set up of the IMAT apparatus was used to image the full monoblock samples. Therefore scanning parameters were identical for all images collected with neutron tomography. To characterise the intrinsic performance of the imaging system a 'Siemens star' test pattern placed in close-contact with the detector was used to measure the modulation transfer function (MTF) [27]. A neutron radiograph of this pattern taken at IMAT with scanning settings consistent with those used for the sample imaging is shown in Figure 19. By this method it was calculated from the MTF that the imaging system would be capable of resolving features greater than 112 µm. This value is smaller in comparison with the geometrical unsharpness reported in Table 4 and therefore could not be further improved experimentally.

The main reason for investigating the use of neutron tomography was to ascertain its capability to image full monoblocks non-destructively. As shown in Figure 10 this was successfully demonstrated on both the ITER_MB and CCFE_MB samples. By comparison with optical microscopy it was found that it was possible to resolve surface features of greater than 250 µm in size. Similarly sized features were observed internally, for example a void found in the braze layer of the in the CCFE_MB sample as shown in Figure 21 and Figure 22. The image resolution impeded measurement of the braze layer thickness which was expected to be around 75 µm, however it was clearly visible at the layer interfaces. It should also be noted that the neutron imaging also displayed a contrast in greyscale level between the CuCrZr of the inner coolant pipe and the Cu of the functional interlayer (see Figure 21). Very little contrast was observed in the X-ray tomography image. For the ITER_MB sample there were no features of interest visible at the W-Cu interface indicating a good join due to no defect being present or that they were smaller than the imaging resolution. An interesting observation was made that the neutron imaging resolved the sample's serial ID which had been the laser etched to a relatively shallow depth on an external surface, as shown in Figure 23. The etching appears brighter in the image (i.e. more highly attenuating) than the bulk W. It is possible that this apparent contrast is either a product of a change in the W microstructure in this region or in its material contamination e.g. due to contamination during the etching process. In general, the level of noise and scanning artefacts was low enough to perform qualitative observations and quantitative measurements.
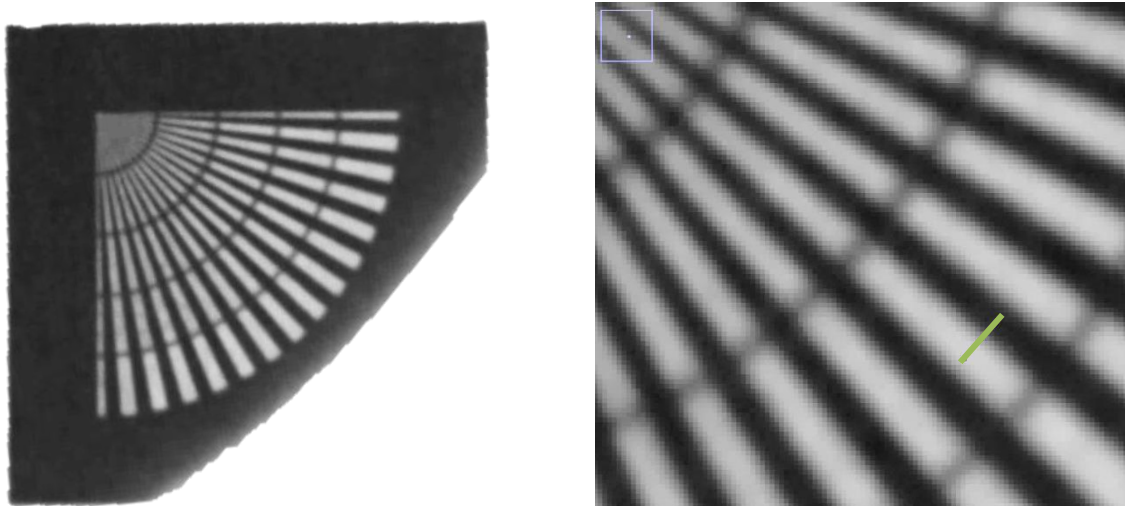
Figure 19. Radiograph of Siemens star (left) with zoomed in region (right) and location of profile line (green) used to calculate modulation transfer function.
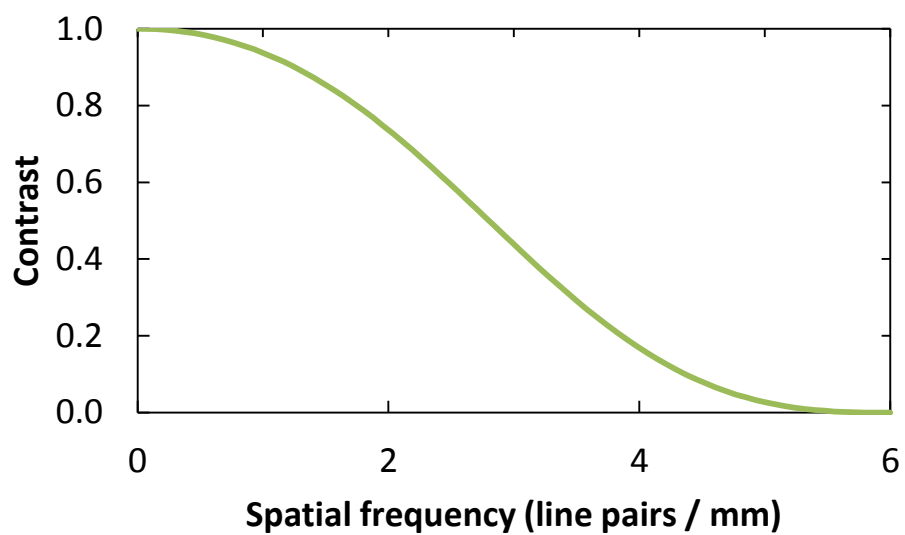

Figure 20. Plot showing contrast with respect to spatial frequency for a neutron radiograph of the 'Siemens star' standard. This curve is used to calculate the modulation transfer function and thus infer the theoretical minimum resolvable feature.
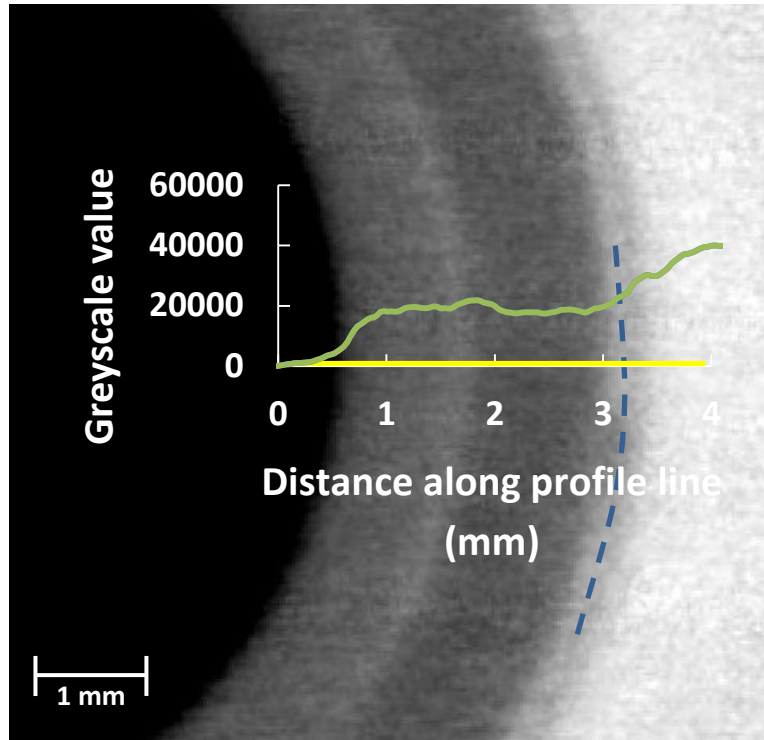
Figure 21. Plot of greyscale values (green) with respect to distance along profile line (yellow). Plot is overlaid on neutron tomographic slice where profile was taken to show direct relation between changes in greyscale and image features. Also shown is (dashed blue) profile line used for Figure 22 to highlight void observed in braze layer.
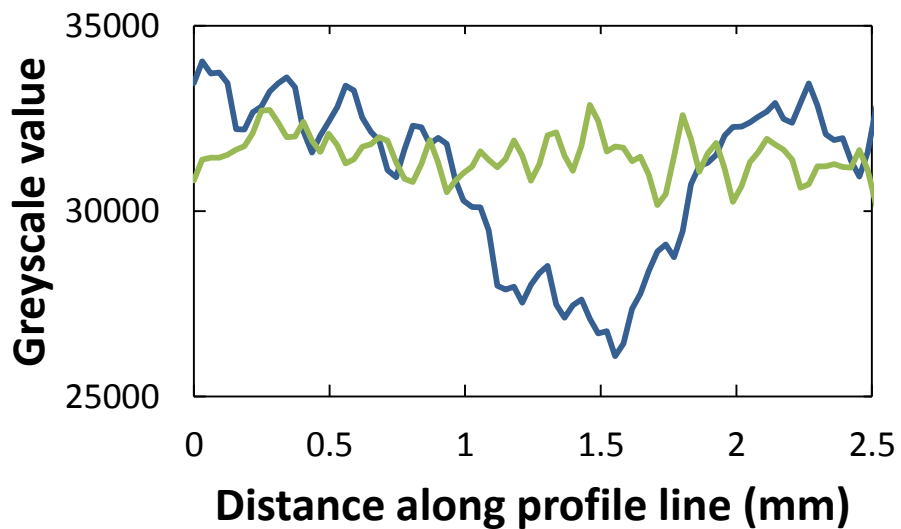

Figure 22. Plot of greyscale values with respect to distance along (dashed blue) profile line from Figure 21. Reduction in greyscale value 1.5 mm along profile line shows location of void in braze layer. For comparison, a second (green) profile line from the same sector but at a greater depth shows the typical variation in greyscale due to image noise.
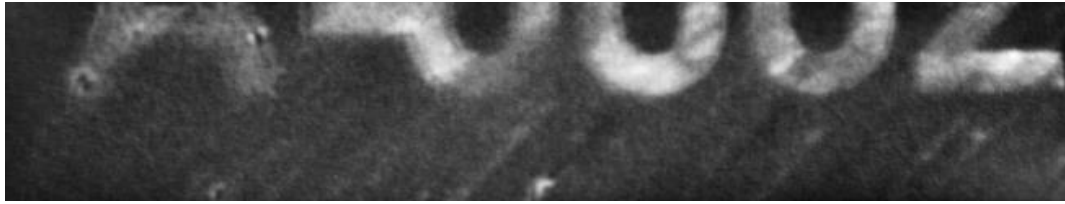
Figure 23. Part of laser etched sample serial ID on outer surface of ITER_MB sample that was visible in neutron tomography image.

In addition to the full monoblock samples, the ROI samples and IPP_Wf-Cu sample scanned by X-ray tomography were also imaged by neutron tomography for direct comparison. All of the samples were successfully scanned with images resolving features of similar size to that of the full MB samples. The images of ITER_MB_ROI and ITER_HHFT_ROI (see Figure 6 and Figure 7, respectively) show a clear interface between the W armour and Cu interlayer. There were no observable features at the W-Cu interface indicating either that none were present or that they were smaller in size than the experimental spatial resolution. There was no observable contrast between the Cu and CuCrZr layers in the ITER_HHFT_ROI sample. Because there was observable contrast in the CCFE sample, this suggests that there exists some compositional difference in either the Cu or CuCrZr materials between the ITER and CCFE samples. The Cu-CuCrZr join in the ITER_HHFT_ROI sample was performed via hot radial pressing and therefore did not require any filler (or braze) material. Because of this there were no markers present to identify the Cu-CuCrZr interface. As the location of the interface was known, by measuring the radial distance it was possible to investigate this region which was found not to contain any observable features (i.e. none were present or they were smaller than the image resolution). When observing the ITER_HHFT_ROI sample in the xz plane it was found that there was a bevel (or chamfer) in the W-Cu interface near the top of the sample (see Figure 25). This is likely to be a by-product of the manufacturing process.

For the CCFE_MB_ROI sample (see Figure 8) the features observable were similar to that of the CCFE_MB samples. That is, the braze layer and some defects within this could be seen but the resolution wasn't sufficient to measure the braze thickness. This was expected due to identical scanning parameters being used. There was a small reduction in image noise for the CCFE_MB_ROI sample. Figure 24 shows a comparison of a similar region in the two samples. Again a contrast in greyscale levels was observed between the Cu and CuCrZr layers.
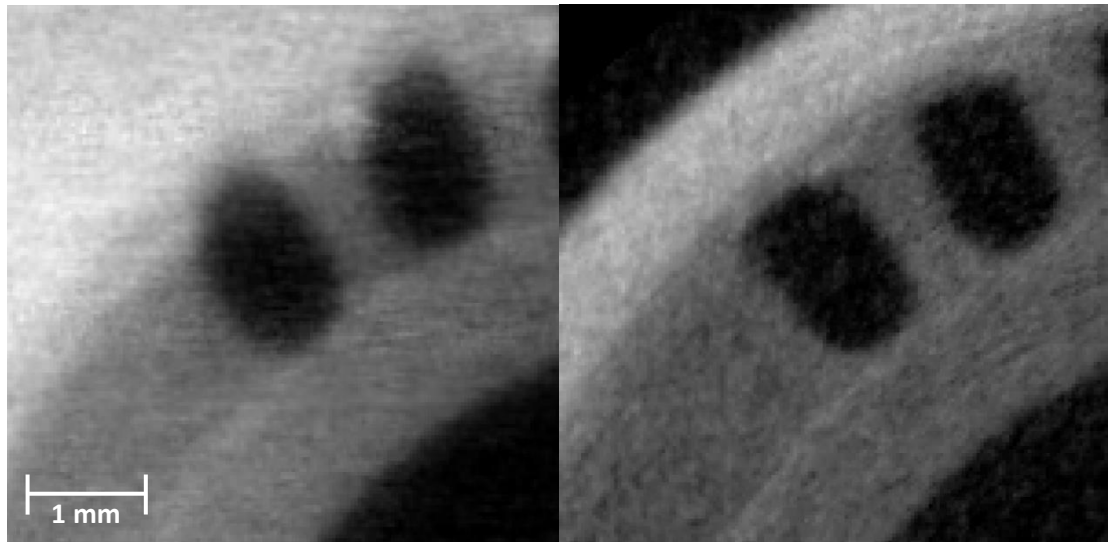
Figure 24. Zoomed in xy plane images from neutron tomography images of the (left) CCFE_MB and (right) CCFE_MB_ROI samples for comparison.

The 150 µm diameter of the W fibres in the IPP_Wf-Cu was greater than the geometric unsharpness of 88 µm meaning that it was expected that the fibres would be observable, as is indeed the case. In the xy plane, crossing the fibre diameter, defining the fibre-matrix boundary is challenging because of the image noise (see Figure 26). However, in the radial direction the definition is clearly visible (see Figure 27) and can be used to investigate fibre placement (see Figure 28). It should be noted that, although noise is present, there is distinct contrast in the greyscale levels of the background air, Cu matrix and W fibres. This contrast was not present in the equivalent X-ray tomography image. Additionally there are no streaking artefacts emitting from the W fibre edges. This image is sufficient for qualitative observation of the fibres but does not have adequate resolution to investigate the fibre-matrix interface.
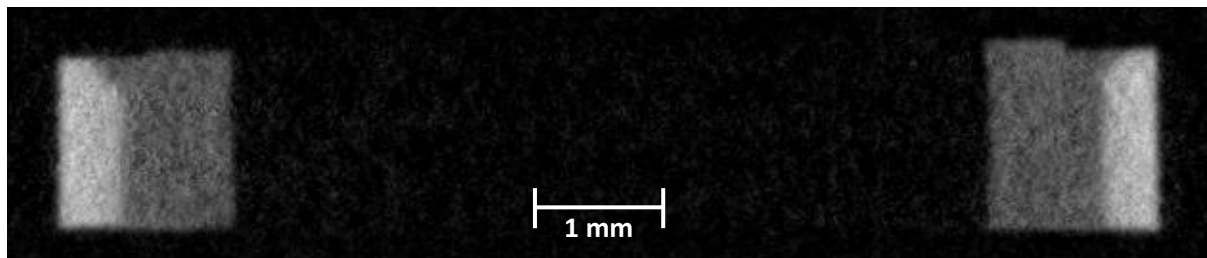

Figure 25. Cross sectional neutron tomography slices from the xz plane for the ITER_HHFT_ROI sample.
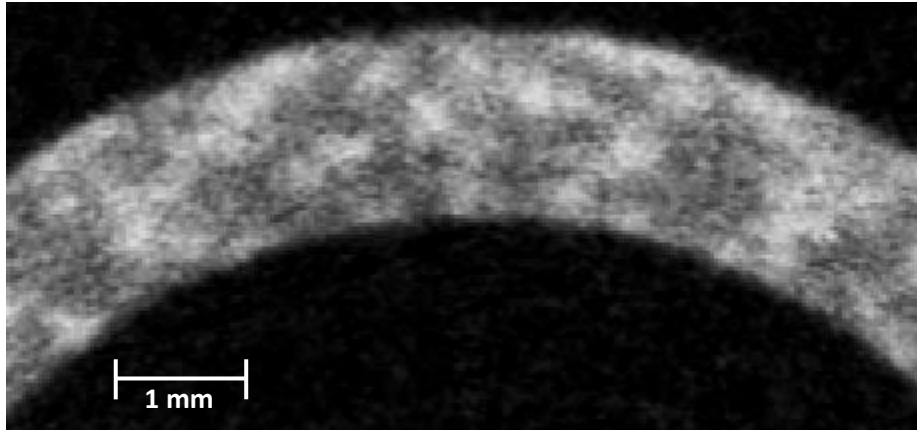
Figure 26. Zoomed in xy plane image from neutron tomography image of IPP_Wf-Cu sample.
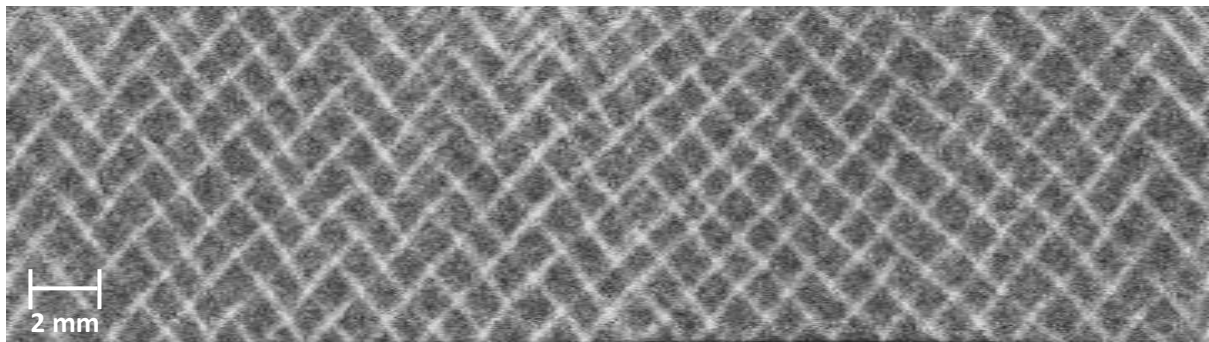

Figure 27. 'Unrolled' section from neutron tomography image of IPP_Wf-Cu sample at radius = 5.75 mm (i.e. x-axis is along θ and y-axis is along length of pipe).
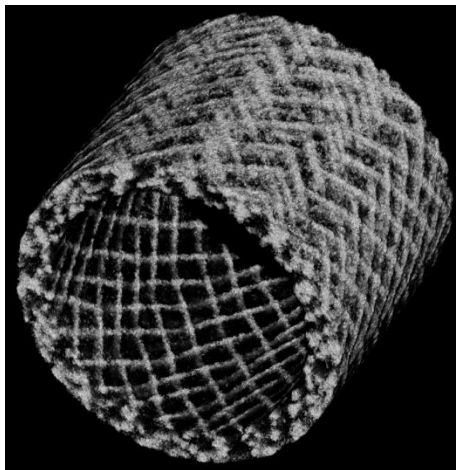

Figure 28. 3D visualisation from neutron tomography data of W fibre placement within IPP_Wf-Cu sample, Cu matrix has been made transparent to assist viewing.

6.4. Comparison of X-ray and neutron tomography data

Despite W being a relatively high attenuator of X-rays and neutrons, both tomography methods were shown capable of imaging samples containing W, albeit with varying degrees of success.

A few key logistical aspects differentiate the techniques. Because X-ray tomography is less penetrating of W it was required to machine the MBs into ROI samples. An obvious disadvantage of this approach is that, by removing a layer of the armour, this use of X-ray tomography is no longer a

non-destructive testing (NDT) method. If to be used during manufacturing production, this would restrict its use to batch sampling. Comparatively, neutron tomography of full MB was possible and the resulting images had the same resolution as the ROI samples which means it may be used as a NDT method.

X-ray tomography equipment is increasingly becoming an industry standard technique for NDT, therefore equipment is readily available and comparatively cheap. However, neutron tomography is currently only available at select facilities globally which impacts operational costs. The current cost of purchasing an X-ray CT scanner is approximately equivalent to 50-100 days of neutron tomography operational costs as a service. The low availability and increased cost of neutron tomography may be prohibitive in scanning large numbers of MBs. Demonstrated here was the ability to scan multiple samples in one neutron tomography scan when stacked upon each other. This would be appropriate for scanning monoblock assemblies rather than individual samples. Another consideration when using neutron tomography is that samples become activated through interaction with the neutrons. The amount of waiting time required before samples may then be transported depends on the length of time the sample is left in the neutron beam. For the scans in this study this was of the order of weeks, but the level of activity is low and samples may be handled manually.

For the ROI samples the ITER_MB_ROI and ITER_HHFT_ROI X-ray tomography images contained such a high level of artefacts that they were unusable. The increase in the maximum attenuation path through these samples was 60 % and 4 %, respectively, compared with the CCFE_MB_ROI sample. The thickness of the W layer in both the ITER_HHFT_ROI and CCFE_MB_ROI samples was 0.5 mm but the total W volume was greater for the ITER_HHFT_ROI sample. It is therefore apparent that the quality of the resultant X-ray tomography image is highly sensitive to the amount of tungsten in the sample due to its high level of X-ray attenuation. If a sufficient volume of W is removed it is possible to obtain a valuable 3D image via X-ray tomography.

By directly comparing the X-ray and neutron tomography images for the CCFE_MB_ROI sample it is clear that the X-ray image provided valuable additional resolution and less noise. Smaller features were observable and those visible in both methods could more accurately be quantitatively measured with X-ray tomography. However, this was the only sample where this was proven true meaning if X-ray tomography was to be used provisions must be made to reduce the X-ray attenuation path through W. The neutron tomography was shown to provide adequate image detail to perform qualitative observations for all samples. Therefore, both scanning techniques are useful but with different benefits. It would be more appropriate to use the higher resolution X-ray tomography for the research and development cycle where samples may be tested destructively and neutron tomography for quality assurance of manufactured assemblies.

Recently hardware developments have seen the introduction of higher energy X-ray tomography scanners [28]. It is possible that these would allow increased length of attenuation paths through W. This is likely to be a modest increase that would still require the production of ROI samples.

7. Conclusions

A comparative study was performed using X-ray and neutron tomography to investigate the appropriateness of the techniques to inspect the manufacturing of a heat exchanger component for

a fusion energy device. It was demonstrated that both techniques were capable of imaging components which included tungsten which is a relatively high attenuator of X-rays and neutrons. Each technique had its own benefits and drawbacks.

X-ray tomography was shown to be highly sensitive to the length of the maximum attenuation path through tungsten. Thus it was required to machine region of interest samples from larger components for investigations. In this instance investigations focussed on the quality of the joining interface between the inner Cu alloy coolant pipe and outer W armour. In samples where sufficient tungsten was removed the resulting image had relatively high resolution (features of 60 μm or greater were observable) and value for qualitative and quantitative analysis. Where insufficient tungsten was removed images were effectively unusable.

Due to the differences in the neutron tomography technique, images will have a lower baseline resolution than what is possible with X-ray tomography. However, the reason for using neutron tomography is for when X-ray tomography is not possible due to large signal attenuation e.g. full components. As such, the main goal for using neutron tomography was to demonstrate the feasibility of using the technique as a non-destructive method (i.e. removing the need to produce 'region of interest' samples). This was successfully demonstrated on full heat exchanger components (divertor monoblock). For a direct comparison with the X-ray tomography, the 'region of interest' samples were also imaged. As expected, the resulting resolution was lower that X-ray tomography ranging from 88 μm to 176 μm for the IPP_Wf-Cu and ITER_MB samples, respectively. However they could be used non-destructively and yielded images adequate for quality assurance. It is believed that this is the first time that a full tungsten divertor monoblock has been imaged by computerised tomography.

If used appropriately, both these tomography methods can produce valuable data either for the research and development cycle of fusion component design or in quality assurance of manufacturing.

8. Acknowledgements

9. References

[1]   A. S. Kukushkin, H. D. Pacher, V. Kotov, G. W. Pacher, and D. Reiter, "Finalizing the ITER divertor design: The key role of SOLPS modeling," *Fusion Eng. Des.*, vol. 86, no. 12, pp. 2865–2873, 2011.

[2]   M. Merola and G. Vieider, "On the use of flat tile armour in high heat flux components," *J. Nucl. Mater.*, vol. 258–263, pp. 672–676, Oct. 1998.

[3]   "The virtual vessel – cutaway with plasma." [Online]. Available: https://www.euro-fusion.org/2011/08/the-virtual-vessel/?view=gallery-11. [Accessed: 25-Jul-2016].

[4]   "ITER / Photos / Technical." [Online]. Available: https://www.iter.org/album/Media/7 - Technical. [Accessed: 02-Oct-2017].

[5]   J. H. You, G. Mazzone, E. Visca, C. Bachmann, E. Autissier, T. Barrett, V. Cocilovo, F. Crescenzi, P. K. Domalapally, D. Dongiovanni, S. Entler, G. Federici, P. Frosi, M. Fursdon, H. Greuner, D. Hancock, D. Marzullo, S. McIntosh, A. V. Müller, M. T. Porfiri, G. Ramogida, J. Reiser, M. Richou, M. Rieth, A. Rydzy, R. Villari, and V. Widak, "Conceptual design studies for the European DEMO divertor: Rationale and first results," *Fusion Eng. Des.*, vol. 109–111, no. PartB, pp. 1598–1603, 2016.

[6]   R. A. Pitts, S. Carpentier, F. Escourbiac, T. Hirai, V. Komarov, S. Lisgo, A. S. Kukushkin, A. Loarte, M. Merola, A. Sashala Naik, R. Mitteau, M. Sugihara, B. Bazylev, and P. C. Stangeby, "A full tungsten divertor for ITER: Physics issues and design status," *J. Nucl. Mater.*, vol. 438, pp. S48–S56, Jul. 2013.

[7]   Y. Zhang, A. Galloway, J. Wood, M. B. O. Robbie, D. Easton, and W. Zhu, "Interfacial metallurgy study of brazed joints between tungsten and fusion related materials for divertor design," *J. Nucl. Mater.*, vol. 454, no. 1–3, pp. 207–216, Nov. 2014.

[8]   S. Cao, C. Somsen, M. Croitoru, D. Schryvers, and G. Eggeler, "Focused ion beam/scanning electron microscopy tomography and conventional transmission electron microscopy assessment of Ni4Ti3 morphology in compression-aged Ni-rich Ni–Ti single crystals," *Scr. Mater.*, vol. 62, no. 6, pp. 399–402, Mar. 2010.

[9]   S. Roccella, G. Burrasca, E. Cacciotti, A. Castillo, A. Mancini, A. Pizzuto, A. Tatì, and E. Visca, "Non-destructive methods for the defect detection in the ITER high heat flux components," *Fusion Eng. Des.*, vol. 86, no. 9–11, pp. 1791–1796, Oct. 2011.

[10]   M. Richou, A. Durocher, M. Medrano, R. Martinez-Oña, J. Moysan, and B. Riccardi, "Data merging of infrared and ultrasonic images for plasma facing components inspection," *Fusion Eng. Des.*, vol. 84, no. 7–11, pp. 1593–1597, Jun. 2009.

[11]   Ll. M. Evans, L. Margetts, V. Casalegno, F. Leonard, T. Lowe, P. D. Lee, M. Schmidt, and P. M. Mummery, "Thermal characterisation of ceramic/metal joining techniques for fusion applications using X-ray tomography," *Fusion Eng. Des.*, vol. 89, pp. 826–836, 2014.

[12]   S. E. Pryse and L. Kersley, "A preliminary experimental test of ionospheric tomography," *J. Atmos. Terr. Phys.*, vol. 54, no. 7–8, pp. 1007–1012, Jul. 1992.

[13]   U. Hampel, "6 – X-ray computed tomography," in *Industrial Tomography*, 2015, pp. 175–196.

[14]   A. Zivelonghi, T. Weitkamp, and A. Larrue, "Open porosity and 3D pore architecture in plasma-sprayed tungsten," *Scr. Mater.*, vol. 115, pp. 66–70, Apr. 2016.

[15]   M. Strobl, I. Manke, N. Kardjilov, A. Hilger, M. Dawson, and J. Banhart, "Advances in neutron radiography and tomography," *J. Phys. D. Appl. Phys.*, vol. 42, no. 24, p. 243001, Dec. 2009.

[16]   M. Fursdon, T. Barrett, F. Domptail, Ll. M. Evans, N. Luzginova, N. H. Greuner, J.-H. You, M. Li, M. Richou, F. Gallay, and E. Visca, "The development and testing of the thermal break divertor monoblock target design delivering 20 MW m −2 heat load capability," *Phys. Scr.*, vol. T170, no. T170, p. 14042, Dec. 2017.

[17]   A. v. Muller, D. Ewert, A. Galatanu, M. Milwich, R. Neu, J. Y. Pastor, U. Siefken, E. Tejado, and J. H. You, "Melt infiltrated tungsten–copper composites as advanced heat sink materials for plasma facing components of future nuclear fusion devices," *Fusion Eng. Des.*, vol. 124, pp.

455–459, Nov. 2017.

[18]   A. C. Kak and M. Slaney, *Principles of Computerized Tomographic Imaging*. Society for Industrial and Applied Mathematics, 2001.

[19]   British Standard, "Non destructive testing - Radiation methods - Computed tomography - Part 2: Principle, equipment and samples," pp. 1–21, 2011.

[20]   British Standard, "Non destructive testing — Radiation methods — Computed Tomography Part 3: Operation and interpretation," no. September 2011, 2011.

[21]   T. Minniti, W. Kockelmann, G. Burca, J. F. Kelleher, S. Kabra, S. Y. Zhang, D. E. Pooley, E. M. Schooneveld, Q. Mutamba, J. Sykora, N. J. Rhodes, F. M. Pouzols, J. B. Nightingale, F. Aliotta, L. M. Bonaccorsi, R. Ponterio, G. Salvato, S. Trusso, C. Vasi, A. S. Tremsin, and G. Gorini, "Materials analysis opportunities on the new neutron imaging facility IMAT@ISIS," *J. Instrum.*, vol. 11, no. 3, pp. C03014–C03014, Mar. 2016.

[22]   W. Kockelmann, G. Burca, J. F. Kelleher, S. Kabra, S. Y. Zhang, N. J. Rhodes, E. M. Schooneveld, J. Sykora, D. E. Pooley, J. B. Nightingale, F. Aliotta, R. C. Ponterio, G. Salvato, D. Tresoldi, C. Vasi, J. B. McPhate, and A. S. Tremsin, "Status of the Neutron Imaging and Diffraction Instrument IMAT," in *Physics Procedia*, 2015, vol. 69, pp. 71–78.

[23]   T. Minniti, K. Watanabe, G. Burca, D. E. Pooley, and W. Kockelmann, "Characterization of the new neutron imaging and materials science facility IMAT," *Nucl. Instruments Methods Phys. Res. Sect. A Accel. Spectrometers, Detect. Assoc. Equip.*, vol. 888, pp. 184–195, Apr. 2018.

[24]   V. Finocchiaro, F. Aliotta, D. Tresoldi, R. C. Ponterio, C. S. Vasi, and G. Salvato, "The autofocusing system of the IMAT neutron camera," *Rev. Sci. Instrum.*, vol. 84, no. 9, p. 93701, Sep. 2013.

[25]   J. Schindelin, I. Arganda-Carreras, E. Frise, V. Kaynig, M. Longair, T. Pietzsch, S. Preibisch, C. Rueden, S. Saalfeld, B. Schmid, J.-Y. Tinevez, D. J. White, V. Hartenstein, K. Eliceiri, P. Tomancak, and A. Cardona, "Fiji: an open-source platform for biological-image analysis.," *Nat. Methods*, vol. 9, no. 7, pp. 676–82, Jun. 2012.

[26]   J. Schindelin, C. T. Rueden, M. C. Hiner, and K. W. Eliceiri, "The ImageJ ecosystem: An open platform for biomedical image analysis," *Mol. Reprod. Dev.*, vol. 82, no. 7–8, pp. 518–529, Jul. 2015.

[27]   E. L. Nickoloff and R. Riley, "A simplified approach for modulation transfer function determinations in computed tomography," *Med. Phys.*, vol. 12, no. 4, pp. 437–442, Jul. 1985.

[28]   H. Villarraga-Gómez, "Seeing is Believing: X-ray Computed Tomography for Quality Control," *Quality*, vol. 55, no. 6, pp. 21–23, 2016.